Lateral diffusivity coefficients from the dynamics of a SF_6 patch in a coastal environment.

M. Kersalé[a,*], A. A. Petrenko[b,c], A. M. Doglioli[b,c], F. Nencioli[d], J. Bouffard[e], S. Blain[f,g], F. Diaz[b,c], T. Labasque[h], B. Queguiner[b,c], I. Dekeyser[b,c]

[a] *Laboratoire de Physique des Océans, UMR 6523 CNRS-Ifremer-IRD-UBO, Université de Bretagne Occidentale, Brest, France*
[b] *Aix Marseille Université, CNRS/INSU, IRD, MIO, UM 110, 13288 Marseille, France.*
[c] *Université de Toulon, CNRS/INSU, IRD, MIO, UM 110, 83957 La Garde, France.*
[d] *Plymouth Marine Laboratory, Prospect Place, The Hoe, Plymouth PL1 3DH, United Kingdom.*
[e] *RHEA for ESA/ESRIN, via Galileo Galilei 2 , 00044 Frascatti, Italy.*
[f] *Sorbonne Universités, UPMC Univ Paris 06, UMR7621, Laboratoire d'Océanographie Microbienne, Observatoire Océanologique, 66650 Banyuls/mer, France.*
[g] *CNRS, UMR7621, Laboratoire d'Océanographie Microbienne, Observatoire Océanologique, 66650 Banyuls/mer, France.*
[h] *Université de Rennes 1, Géosciences Rennes, UMR CNRS 6118, 35042 Rennes, France.*

Abstract

The dispersion of a patch of the tracer sulfur hexafluoride (SF_6) is used to assess the lateral diffusivity in the coastal waters of the western part of the Gulf of Lion (GoL), northwestern Mediterranean Sea, during the Latex10 experiment (September 2010). Immediately after the release, the spreading of the patch is associated with a strong decrease of the SF_6 concentrations due to the gas exchange from the ocean to the atmosphere. This has been accurately quantified, evidencing the impact of the strong wind conditions during the first days of this campaign. Few days after the release, as the atmospheric loss of SF_6 decreased, lateral diffusivity coefficient at spatial scales of 10 km has been computed using two approaches. First, the evolution of the patch with time was combined with a diffusion-strain model to obtain estimates of the strain rate (γ=2.5 10^{-6} s^{-1}) and of the lateral diffusivity coefficient (K_h=23.2 m^2 s^{-1}). Second, a steady state model was applied, showing K_h values similar to the previous method after a period of adjustment between 2 and 4.5 days. This

*Corresponding author
Email address: marion.kersale@univ-brest.fr (M. Kersalé)

implies that after such period, our computation of K_h becomes insensitive to the inclusion of further straining of the patch. Analysis of sea surface temperature satellite imagery shows the presence of a strong front in the study area. The front clearly affected the dynamics within the region and thus the temporal evolution of the patch. Our results are consistent with previous studies in open ocean and demonstrate the success and feasibility of those methods also under small-scale, rapidly-evolving dynamics typical of coastal environments.

Keywords: Lateral diffusivity coefficient, SF_6 tracer, Lagrangian referential, Coastal ocean

2014 MSC: 00-01, 99-00

---

1. Introduction

One of the major challenges in the studies of ocean dynamics and mixing lies in estimating the dispersion of particles by turbulent processes. To describe it, classic theoretical studies have introduced the eddy diffusion coefficient, K_h, which parametrizes the effects of small scale turbulence. This coefficient is analogous to the one in Fick's first law of diffusion; however, it is associated to the mixing induced by small turbulence, rather than to molecular diffusion. The early study of [1] has showed that K_h depends on the length scale of the parametrized turbulent processes, introducing the concept of scale-dependent dispersion. In the following years, this scale dependence was confirmed by several experiments at sea by [2, 3, 4].

K_h is a key parameter for the turbulent closure schemes of both global and regional numerical models. The simplest closure schemes usually assume isotropic, constant horizontal eddy diffusivity; more complex ones are based on spatio-temporally varying K_h, which depends on the dynamical characteristics of the resolved large scale processes [e.g. 5, 6, 7]. The accurate tuning of the values of eddy diffusivity is a key aspect for numerical experiments, since they strongly control the dispersion of physical and biogeochemical tracers [8]. Thus, in situ estimates of K_h provide crucial information for improving the performance and accuracy of ocean models.

Within the last decade the number of quantitative estimates of the scale-dependent K_h from *in situ* observations have increased with technological advancements. However, such quantifications still represent an observational challenge due to the small dimensions and short duration associated with turbulent processes. Estimates of K_h can be obtained from Eulerian or Lagrangian approaches. Generally, Eulerian estimates are obtained from remote sensing analysis [9, 10], while Lagrangian studies have been developed to calculate this coefficient in situ. Lagrangian-based estimates of K_h can be derived from the trajectories of freely drifting instruments, like surface drifters and subsurface floats [11] (for a extensive overview of the methods, see [12]). Eddy dispersion coefficients derived

from these methods are characteristics of oceanic mesoscale processes (length scales of ~10-100 km). In the last years, advancements in drifter technology, have favored the development of Lagrangian studies specifically designed to investigate coastal dynamics at smaller temporal and spatial scales [*e.g.* 13, 14, 15]. Such studies have helped improving our understanding of the contribution of local and non-local processes in regulating relative dispersions at scales below the Rossby radius of deformation. Furthermore, the quantification of K_h at the submesoscale has been recently investigated by [16].

The determination of K_h, associated to smaller scales, has been usually developed from experiments based on inert tracers. Among various types of tracer, fluorescent dyes, especially Rhodamine B, have been largely used to study turbulent diffusion [17]. Although numerous dye experiments have also been performed in coastal environment or fresh water lakes, very few of these studies have been made in stratified coastal areas with strong mesoscale activity. Noteworthy exceptions include the rhodamine dye experiments in the Massachusett Bay [18] and the Coastal Mixing and Optics (CMO) project [19]. Dye experiments have been deployed in the stratified thermoclines of the Celtic Sea on the NW European Shelf by [20] and [21] and in the northern Monterey Bay, California by [22].

The sulfur hexafluoride (SF_6), a stable and inert gas detectable at concentrations a million times lower than dyes, has been mainly used for open ocean tracer experiments. The main advantage of the SF_6 is that, due to its low background concentration in seawater, it can be used via small injections of SF_6 saturated seawater [26]. Nevertheless its low solubility in water makes it more difficult to inject than dye tracers. Since the mid 1980s, SF_6 has been widely employed in horizontal turbulent processes studies. More recently CF_3SF_5 (trifluoromethyl sulfur pentafluoride), with same properties and behavior, has emerged as a viable alternative to SF_6 for large scale experiment [23, 24, 25]. Since the successful test release of CF_3SF_5 had not yet been undertaken during the implementation of the project, we used SF_6 rather than CF_3SF_5.

Lateral diffusivities at scales smaller than 100 km have been obtained during

various SF_6 tracer experiments (NATRE,[26] ; IronEx-I, [27] ; SOIREE, [28] ; PRIME, [29]). Such estimates are based on the hypothesis that, under local mesoscale stirring (which can be approximated, to a first order, as 2-dimensional and divergence-free), the initial shape of the tracer patch will elongate along one direction while thinning along the other. The width of the patch will keep decreasing until the effects of mesoscale stirring are balanced by smaller scale diffusion and an equilibrium is reached. Thus, lateral diffusivity can be computed by combining estimates of the strain rate with *in situ* measurements of the patch width. Strain rate is usually estimated from successive *in situ* mappings [26] or from the analysis of satellite imagery of surface tracers (*e.g.* chlorophyll-a concentration [28]). Lateral diffusivities computed using this approach range from 0.5 to 25 $m^2\ s^{-1}$ for tracer filaments with widths between 1 and 10 km. At similar scales but in lower energetic systems, lateral diffusivities have also been estimated (from SF_6 in the Santa Monica Basin Tracer Experiment, [30] and from CF_3SF_5 in the BATRE one, [25]) by neglecting the strain and measuring the growth of the roughly circular tracer patch. Following this method, the lateral diffusivities were of the order of 10 $m^2\ s^{-1}$ for the interior of the two basins at scales on the order of 10 km.

Estimates of lateral diffusivities can be used to understand the dynamics and mixing within specific water patches, and therefore to assess the rates of some biogeochemical processes. In the case of biogeochemical applications, SF_6 has been used to estimate deep-water ocean ventilation, pathways, and anthropogenic CO_2 uptake [31, 32, 33]. During the PRIME project (Plankton Reactivity In the Marine Environment), the evolution of an SF_6 patch has allowed a quantitative understanding of the nutrient supply into the mixed layer of an anticyclonic eddy in the North Atlantic [29, 34]. Combined with iron enrichment, the SF_6 tracer has provided the potential to assess ecosystem responses to added iron [35, 36, 37, 38, 39].

As mentioned before, SF_6 has been rarely used in coastal areas, where the circulation is usually complex due to the influence of different forcings (local atmospheric conditions, tides, freshwater inputs) and the constraints imposed

on the flow by its coastline and bathymetry [40]. Coastal dynamics is critical for regulating the cross-shore exchange of materials between continents and oceans. The study of its functioning is therefore of considerable interest for understanding the coupling of terrestrial and oceanic biogeochemical cycles. Two SF_6 experiment have been conducted in the Florida shelf [41] and near South Georgia [42]. Given the success of these first SF_6 tracer experiments, our study explores the application of SF_6 in a coastal area of the North Western Mediterranean Sea where several in situ data have been collected within the framework of the LATEX project (LAgrangian Transport EXperiment, 2007-2011 ; `http://www.mio.univ-amu.fr/LATEX`).

The LATEX project aimed to investigate the role of coupled physical and biogeochemical dynamics at the mesoscale in regulating the exchanges of matter and energy between inshore and offshore areas. One of the goals of the project was to analyze transport patterns and diffusion rates in the western part of the Gulf of Lion (GoL). The GoL is located in the northwestern Mediterranean Sea and is characterized by a relatively large continental margin (Fig. 1-a). Its hydrodynamics is complex and highly variable in space and time [43]. Its circulation is strongly influenced by the southwestward along-slope Northern Current (NC). This density current flows in a cyclonic way and constitutes an effective dynamical barrier isolating the coastal waters of the continental shelf from the open northwestern Mediterranean Sea [44, 45, 46]. Cross-shore exchanges between the GoL and offshore waters are mainly regulated by wind induced dynamics [47, 48], and by processes associated with the NC, such as intrusion into the continental shelf, barotropic and baroclinic instabilities arising along its internal and external borders and seasonal modulation of its intensity and position [49, 50, 51].

Two of the four LATEX field campaigns were dedicated to the SF_6 tracer release experiment. The first one, the Latex00 campaign (9-11 June 2007, aboard the R/V Téthys II), was part of a pilot project that aimed to measure the background concentration of SF_6 and to test the Lagrangian navigation software [LATEXtools, 52]. The last one, the Latex10 campaign (1-24 September

2010, aboard the R/V Le Suroît and the R/V Téthys II), investigated the transport structures in the western GoL with an adaptive sampling strategy, which combined satellite data, ship-based ADCP measurements, iterative Lagrangian drifter releases. The sampling strategy enabled the identification of a frontal jet, 10 km-wide, roughly parallel to the coast, along which waters from the continental shelf left the gulf towards the Catalan Basin [53].

The aim of the present work is to use the observations from the Latex10 passive tracer experiment to evaluate the lateral diffusivity coefficient in a coastal area (between depths of 100 and 1000 m), marked by the presence of an energetic small scale dynamical features. The methods to release and measure the SF_6 data are described in Section 2, while the analysis and evolution of the SF_6 patch are showed in Section 3. Air-sea gas exchanges are described in Section 4. In Section 5, the different methods for calculating the lateral diffusivity coefficients, their limits and their applications in the GoL are presented. The estimated coefficients, the temporal evolution of the patch and the air-sea gas exchanges are discussed in Section 6.

2. SF6 release and measurements

A satured SF_6 solution was prepared at the beginning of the Latex10 campaign. A 7000 L steel tank was filled with sea water in the afternoon of September 2. An acrylic cylinder was placed on the top of the tank, making a headspace of about 5 L for effective bubbling. Pure SF_6 gas was injected into the seawater in the tank for 48 h to obtain a saturated SF_6 solution. For determining SF_6 concentrations in the tank before injection, a headspace extraction and a classical gas chromatograph (GC) equipped with a thermal conductivity detector (TCD) were used. The GC/TCD analysis of extracted gas were based on the [54] method. The measured SF_6 concentration was 1.63 10^{-4} mol L^{-1} for the first 4000 L released. Due to a technical problem, the SF_6 concentration decreased to 0.69 10^{-4} mol L^{-1} for the remaining 3000 L. Lateral and vertical homogeneities in the distribution within the area are still a primary assumption, with or without this technical problem. Such hypothesis was likely respected, since the analysis was performed only after a period of 2 days after the release, as in [55].

In order to release the tracer as homogeneously as possible in the horizontal and, thus, study the lateral diffusivity of the tracer patch while minimizing the contribution due to the advection, it was necessary to coordinate the release of the SF_6 in a Lagrangian reference frame. This task was accomplished using the software package LATEXtools [52], that provided information to direct the ship route during the tracer release. The center of the Lagrangian reference frame was defined by the position of a buoy (which is hereafter referred to as the "reference buoy") drogued at 11.5 m depth and deployed at 42°45,01'N - 3°30,11' E (Fig. 1-b) at the beginning of the tracer release on September 11. The reference buoy was equipped with an Iridium transmitter/receiver which ensured the acquisition of its position every 15 minutes. The position of the Lagrangian reference frame and, accordingly, the ship trajectory were adjusted after each acquisition. From the R/V Le Suroît, the satured SF_6 solution was released at a ship speed of 4 knots for a period of 14 h (Table 1). The reconstructed vessel

track in the Lagrangian reference frame matched almost perfectly the planned route [See Figure 6 in 52]. Unfortunately, during the cruise the atmospheric conditions were particularly rough (wind gust exceeding 30 m s^{-1}, Fig. 5-a). In order to prevent as much as possible a quick loss and dispersion of the tracer, the location of the release has been chosen on the basis of the information coming from the weather-forecast model Aladin and a 10-year realistic simulation from a high-resolution ocean circulation model [56]. Indeed, we chose to release the SF_6 during the predicted period of low winds (which indeed turned out to be lower than 10 m s^{-1}, Fig. 5-a) and at the point of current speed minimum as determined in the historical archive of our numerical simulations for similar dynamical and meteorological forcings.

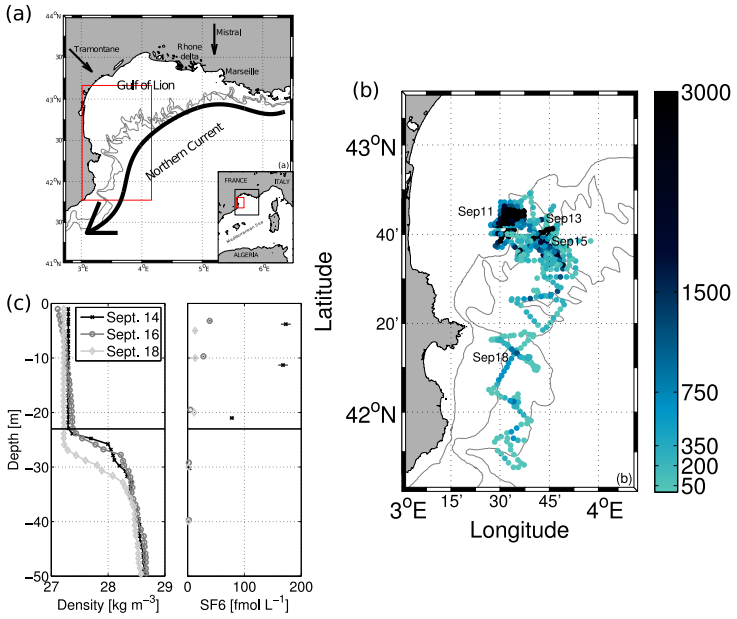

Figure 1: (a) Bathymetry of the Gulf of Lion (200 and 500 m isobaths). Black arrows indicates the Northern Current, and the Tramontane and Mistral winds. The red rectangle indicates the region of focus of the Latex10 campaign. (b) Map of the SF_6 patch, color-coded by SF_6 concentrations [fmol L^{-1}] and marked on selected dates. Isobaths at 100, 200 and 1000 m are plotted with thin lines. (c) Vertical profiles of density [kg m^{-3}] and SF_6 concentrations [fmol L^{-1}] on September 14, September 16 and September 18.

A SF_6 background value of about 1.35 fmol L^{-1} (fmol=10^{-15} mol) estimated during the Latex00 campaign. Such value was used as a reference to design the Latex10 release system and the sampling strategy. Further measurements performed during the Latex10 campaign confirmed that, although slightly higher, background SF_6 concentrations at the time of the experiment were of the same order of magnitude (average equal to 1.72 fmol L^{-1}). In total, 7000 L of SF_6-saturated seawater were released at 7 m depth inside a square area of ~30 km^2. Assuming a rapid vertical redistribution of SF_6 inside the mixed layer, characterized by a depth of about 23 m on September 14 (Fig. 1-c), this release assured the formation of a patch with SF_6 concentrations of about 1250 fmol L^{-1}, 727 times higher than the background value. Based on the volume of injected seawater and the SF_6 concentration inside the tank, the total quantity of SF_6 initially released in the water has been estimated as 0.89±0.12 mol.

After the release, the horizontal evolution of the tracer patch was monitored for 7 days (Fig. 1-b) during a series of 4 successive horizontal mappings at 7 m depth (Table 1). The analytical system used for the measurements of SF_6 was based on continuous flow purge and trap (PT) extraction followed by gas chromatography separation and detection by electron capture detector (GC/ECD ; See Appendix A for a detailed description). This system is different from the previous ones developed by [58] and [59], since it is not based on vacuum sparge sample extraction, but on continuous flow of purified nitrogen for extraction of dissolved gases. The samples were analyzed at a frequency of 6 samples per hour, analogous to previous studies [58]. The uncertainty has been estimated at 5 % for concentrations above the detection limit (0.8 fmol L^{-1}). Moreover, three profiles (six samples per profile) were performed at different stations to ensure the homogeneity of the mixed layer (Fig. 1-c). These profiles revealed a bottom depth of the mixed layer constant with space and time, between 23 and 26 m depth. Concentrations of SF_6 in the mixed layer are reasonably homogeneous (Fig. 1-c). In the presence of a strong gradient, as it is the case at the bottom of the mixed layer depth, the error due to the low resolution of vertical sampling of SF_6 (Niskin bottle) can explain an intermediate value as the one of

78 fmol L^{-1} measured on September 14 at 21 m depth.

In our analysis, the surface SF_6 concentration data have been re-mapped in a Lagrangian reference frame in which the origin moves with the center of mass of the tracer [19]. The spatially irregular data along the ship track are interpolated onto a regular grid using natural neighbor interpolation. This local method, based on the Voronoi diagram [60, 61], has the advantage of accommodating the resolution to the spatial distribution of the initial scattered data.

Table 1: Start and end dates of the release and mapping of the tracer.

	Beginning		End		Time intervals
	Day	Hour (GMT)	Day	Hour (GMT)	
Release	Sept. 11	04h02	Sept. 11	18h00	14 h
Mapping 1	Sept. 11	22h11	Sept. 12	15h49	17.6 h
Mapping 2	Sept. 13	18h40	Sept. 14	12h50	18.2 h
Mapping 3	Sept. 15	18h17	Sept. 16	15h55	21.6 h
Mapping 4	Sept. 18	05h48	Sept. 18	22h03	16.2 h

In the remainder of the study, our analysis of the SF_6 patch is based on the advection-diffusion equation, governing the evolution of the column-integrated, Reynolds-averaged, passive tracer concentration C in an incompressible fluid. Generally, it is based on the hypothesis of a two-dimensional linear strain field in which the strain rate ($\gamma = \frac{\partial u}{\partial x} = -\frac{\partial v}{\partial y}$) varies with time but is homogeneous in space, and the horizontal diffusivity is constant and isotropic. It follows that, the advection-diffusion equation can be written as :

$$\frac{\partial C}{\partial t} + \gamma x \frac{\partial C}{\partial x} - \gamma y \frac{\partial C}{\partial y} = K_h \left(\frac{\partial^2 C}{\partial x^2} + \frac{\partial^2 C}{\partial y^2}\right) - kC\Big|_{z=0} \tag{1}$$

3. SF6 evolution

To evaluate the extension of the patch, we have estimated the SF_6 patch area using two methods. Both are based on the hypothesis that, after the release, SF_6 concentrations within the patches can be approximated by a Gaussian distribution [*e.g.* 28, 19, 39, 62].

230 Following [39], we performed a first estimate of the total area of the patch based on the contour lines concentrations of SF_6. We defined A_{CL} as the area inside the contour lines $[SF_6]_{max}e^{-2}$, with $[SF_6]_{max}$ the maximum concentration of the in situ mapping. Thus, for an idealized Gaussian patch, A_{CL} represents the area where 95.4 % of the total concentration is present. In Fig. 2 the A_{CL} for the four mappings are shown (red lines).

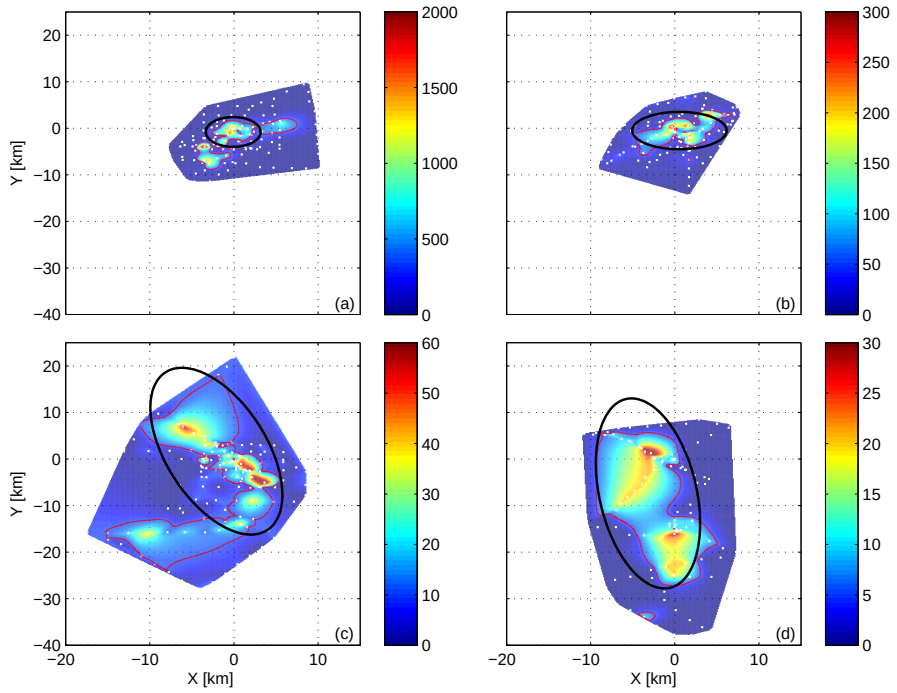

Figure 2: Lagrangian maps of SF_6 concentration [fmol L^{-1}] for Mapping 1 (a), Mapping 2 (b), Mapping 3 (c) and Mapping 4 (d). The plots are referenced to the position of the center mass. Note that the color bar maximum varies with each mapping. The m/e^2 contour lines are shown in red in each plot indicating the patch area with the contour line technique (A_{CL}). Gaussian ellipsoids are shown in black in each plot indicating the fitting patch area (A_{GE}). The locations of SF_6 measurements are indicated by the white dots.

235

For the second method, Gaussian ellipsoids (black ellipsoids, Fig. 2) have been fitted to the horizontal mapping of SF_6 using an unconstrained non-linear optimization. The Gaussian ellipsoids fit are obtained by minimizing the function

for each distribution, starting at an initial estimate and using the Optimization Toolbox routines, which are based on the Nelder-Mead simplex search algorithm [63]. The Gaussian ellipsoids fit can be sensitive to the initial estimate. To better address this aspect, we have varied the initial estimates of the Gaussian ellipsoid, and hence the total number of fits. We have then calculated the averaged values and the standard deviations of the length of the major and minor axis, the center of the ellipse and the angle. With this technique, the area inside the Gaussian ellipsoid ($A_{GE} = \pi\sigma_l\sigma_w$) can be used to calculate a second estimate of the SF_6 patch total area, with σ_l and σ_w the estimated lengths of the semi-major and the semi-minor axis of the SF_6 patch area respectively.

Successive estimates of the SF_6 patch area based on the two techniques (A_{CL}, A_{GE}) are used to analyze the temporal evolution of its spreading (Fig. 3-a). The lengths of the two semi-axis of the patch for each mapping are represented as a function of time in Fig. 3-b and listed in Table 2. For further characterizing the patch geometry, the perimeter of the Gaussian ellipsoid has been calculated with the common Ramanujan method :

$$P = \pi(3(\sigma_l + \sigma_w) - \sqrt{(3\sigma_l + \sigma_w)(\sigma_l + 3\sigma_w)}) \quad (2)$$

If the strain induced by the current remains constant and uniform, the aspect ratio of an initially circular patch, estimated as the ratio Area/Perimeter^2 and scaled using a factor of 4π, would start at 1 and decreases as the patch stretches into a filament. This ratio is represented in Fig. 3-c as a function of time.

Table 2: Estimates of the lengths of the semi-major axis and the semi-minor axis of the SF_6 patch for each mapping.

	σ_l (km)	σ_w (km)
Mapping 1	3.3 ± 1.2	3.2± 1.7
Mapping 2	5.6 ± 2	4± 0.6
Mapping 3	18.4 ± 5.4	6.5± 2.1
Mapping 4	20.5 ± 4.3	5.9± 0.7

We can identify two phases in the temporal evolution of the SF_6 patch. Ini-

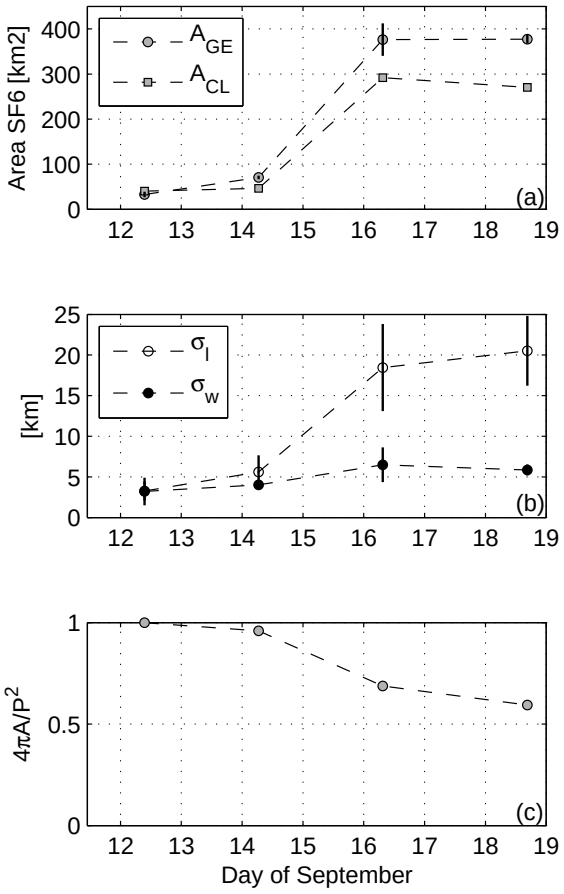

Figure 3: (a) Temporal evolution of the surface area [km^2] of the patch estimated by Gaussian ellipsoids (gray circles - A_{GE}) and m/e^2 contour lines (gray squares - A_{CL}) fitted to the mapped SF_6 data. (b) The lengths of the semi-major (σ_l, white circles) and semi-minor (σ_w, black circles) axis of the Gaussian ellipsoids fitted to the mapped SF_6 data. (c) Aspect ratio of the patch total area (A_{GE}) as area/(perimeter)^2. The ratio is normalized to 1 for an idealized circular patch by multiplying it by 4π. The vertical black lines over the circles (a,b) represent the estimated uncertainties on the calculation of $\sigma_l$and σ_w. They are always calculated for the Gaussian ellipsoids calculations, and thus they are negligible when not visible.

tially, between September 12 to September 14 (Mappings 1 and 2), the patch of tracer spreads slowly in both directions with a small increase of its length and width. During this first phase, the area increases according to both meth-

ods: about 38±2 km^2 for A_{GE} and 6 km^2 for A_{CL} (no errors have been defined in the literature for this method). Within the same period, the SF_6 concentrations decrease of one order of magnitude. Starting from September 14, the semi-major axis of the patch (σ_l) increases quickly, while the semi-minor axis (σ_w) remains approximately constant. During this second phase, the spreading of the patch is anisotropic, with σ_l as much as 3 times the length of σ_w. Strong area increases are observed by both estimates : between Mapping 2 and Mapping 3 A_{GE} (A_{CL} respectively) increases from 70±4 (46) km^2 to 376±90 (292) km^2, corresponding to an area increase of 306±16 (246) km^2, one order of magnitude superior than during the first period. A decrease of the area to perimeter ratio (Fig. 3-c) is observed during both phases, indicating that the patch is progressively stretched into a filament.

Further evidence of this stretching event is obtained by superposing the *in situ* SF_6 concentrations on AVHRR (Advanced Very High Resolution Radiometer) channel 4 imagery provided by Météo-France (Fig. 4). AVHRR channel 4 measurements are usually inaccurate in estimating the absolute values of the sea surface temperature (SST). However, AVHRR channel 4 (hereafter pseudo-SST) imagery has shown to accurately identify the spatial distribution of SST gradients [57, e.g.]. Therefore, pseudo-SST can be successfully used to reconstruct the dynamics of the waters surrounding the patch. On September 12, the tracer patch extends southwestward over the continental shelf (Fig. 1-b), which is characterized by colder surface waters with pseudo-SST around 16°C (Fig. 4-a). After two days, a front between warmer waters from the Northern Current (pseudo-SST~19°C) and colder waters from the shelf is formed along the western continental slope of the gulf (at 4°E - Fig. 4-b). By that time, the tracer patch has slightly drifted eastward toward the western boundary of the front. The dynamical characteristics of the frontal structure detected during the Latex10 campaign have been fully described in the study of [57]. On September 15, the contour line of the total patch area shows a distribution of the tracer elongated along a tongue of colder coastal waters (Fig. 4-c). On September 18, no pseudo-SST satellite image was available due to cloud coverage, when

the tracer is located in front of Cape Creus after a significant southward drift (Fig. 4-d). The analysis of pseudo-SST reveals that the second phase of evolution of SF_6, identified from Fig. 3, is associated with the intense stirring induced by the dynamics of the strong thermal front.

4. Air-sea gas exchange

Other than area and geometry, the patch evolution included variations in SF_6 maximum concentration due to air-sea gas exchange. During the different phases of the temporal evolution of the SF_6 patch, the sink term representing the atmospheric loss (last term in equation (1)) has to be quantified. The maximum concentration of SF_6 decreases from 3000±150 fmol L^{-1} on September 11 (Mapping 1), to 50±2.5 fmol L^{-1} on September 18 (Mapping 4, Fig. 1-b). The SF_6 is an inert tracer, and therefore its dynamics has no internal sources or sinks. Moreover, there are no external sources due to atmospheric input because the patch is supersaturated with respect to the atmosphere. Thus, to investigate the evolution of SF_6 concentration within the mixed layer after its release, two boundary conditions are required : one at the bottom of the mixed layer, and one at the ocean-atmosphere interface. We can consider the exchanges that occur between the mixed layer and the underlying waters to be negligible since, in late summer (the cruise took place in September), the GoL is characterized by a strong stratification. Thus, the bottom boundary condition for the integrated concentration of SF_6 in the mixed layer, hereafter referred to as C, can be written as :

$$K_z \frac{\partial C}{\partial z}\bigg|_{z=z\_mix} = 0 \tag{3}$$

with z_mix the bottom depth of the mixed layer.

The second boundary condition represents the loss of SF_6 at the ocean surface due to the atmospheric loss, and can be expressed as :

$$K_z \frac{\partial C}{\partial z}\bigg|_{z=0} = F = -kC|_{z=0} \tag{4}$$

with F the flux of SF_6 across the air-sea interface (mol m^2 s^{-1}) proportional to $k \equiv k(t)$, the transfer velocity (m s^{-1}).

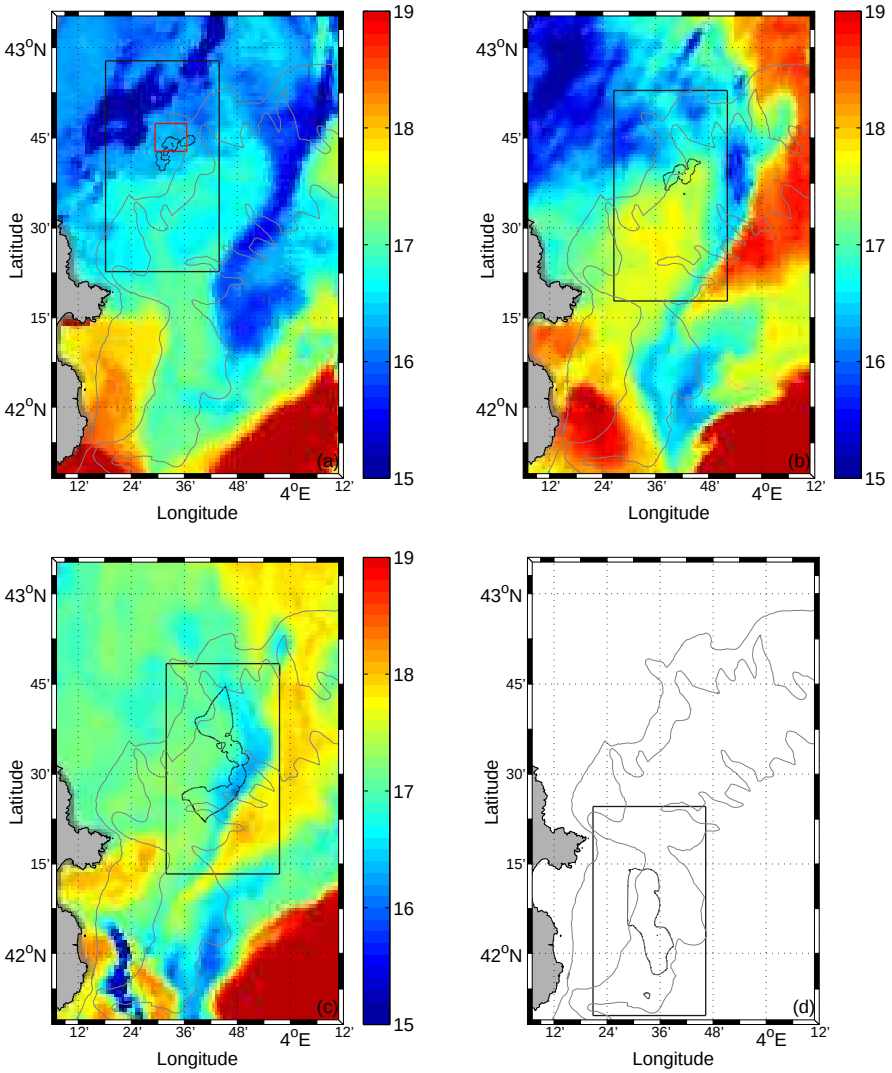

Figure 4: Pseudo-SST satellite image (data from Météo-France) on September 12 (a), September 14 (b), September 15 (c) and Lagrangian contour lines representing the patch area (A_{CL}) for each mapping. On September 18 (d), no pseudo-SST satellite image was available due to the cloud coverage, therefore only Lagrangian contour lines are represented. The small red square (a) represents the initial area of SF_6 release. The black squares correspond to the areas of Fig. 2 for each mapping. Isobaths at 100, 200 and 1000 m are plotted with thin lines.

Making the hypothesis that the surface layer is well mixed over the timescale of concentration decrease due to gas exchange (order of a day), and that dilution processes by mixing and dispersion are first-order processes, equation (1) can be simplified. These processes can be assumed to be first-order processes if the samples are taken well within the tracer patch and if the dilution due to dispersion is of similar or smaller magnitude as/than loss due to gas transfer [55]. Then, the evolution of C with time due to atmospheric loss can be modeled as a negative exponential function:

$$\frac{\partial C}{\partial t} = C_0 - C_0 e^{-\frac{k}{z\_mix}t} \tag{5}$$

with C_0 the released concentration of SF_6 in fmol L^{-1}. The concentration of SF_6 observed at each mapping have been integrated during the entire mapping and over the total patch area in order to estimate the total quantity of SF_6 in mol (black squares - Fig. 5-b).

4.1. Parameterizations of the air-sea transfer velocity

To model this loss, five different parameterizations of the air-sea transfer velocity k can be found in literature. All of them express k as a function of the wind speed at 10 m above the sea level (U_{10}, m s^{-1}). The proposed parameterizations vary depending on the time scales considered. In this work, we use k_{short} for parameterizations based on time scales shorter than 1 day (which also assume steady wind conditions), and k_{long} for parameterizations based on time scales longer than 1 month (which usually use climatological data). In our analysis, we have used hourly U_{10} measured from the ship (Fig. 5-a).

The first formulation of k has been derived in a wind-tunnel experiment by [64] [LM-86 relationship] and then validated by various fields studies. LM-86 relationship is based on short-term winds but involves three sets of values depending on the dynamics regime. These equations propose a piecewise linear

parameterization of k_{short} on wind speed :

$$\begin{cases} k_{short} = 0.17\ U_{10}\ (Sc_{38}/600)^{-2/3} & \text{for } 0\ m\ s^{-1} < U_{10} \leq 3.6\ m\ s^{-1} \\ k_{short} = (2.85\ U_{10} - 9.65)\ (Sc_{38}/600)^{-1/2} & \text{for } 3.6\ m\ s^{-1} < U_{10} \leq 13\ m\ s^{-1} \\ k_{short} = (5.90\ U_{10} - 49.3)\ (Sc_{38}/600)^{-1/2} & \text{for } U_{10} > 13\ m\ s^{-1} \end{cases} \tag{6}$$

where Sc_{38} is calculated with a linear extrapolation of the Schmidt number for seawater with salinity of 35 (Sc_{35}) and fresh water (Sc_0) :

$$\begin{cases} Sc_0 = 3255.3 - 217.13\ T + 6.8370\ T^2 - 0.086070\ T^3 \\ Sc_{35} = 3531.6 - 231.40\ T + 7.2168\ T^2 - 0.090558\ T^3 \end{cases} \tag{7}$$

with T ($^\circ C$) the hourly sea surface temperature data measured by the ship thermosalinometer. The coefficients of equation (7) come from the relationship of [65].

A second parametrization was proposed by [66], who used global ^{14}C calculations to obtain a quadratic dependence of k on either short-term or long-term winds (W-92 relationship) :

$$\begin{cases} k_{short} = 0.31\ U_{10}^2\ (Sc_{38}/660)^{-1/2} \\ k_{long} = 0.39\ U_{10}^2\ (Sc_{38}/660)^{-1/2} \end{cases} \tag{8}$$

[67] have also developed a quadratic parameterization (Ho-06 relationship) for high short-term wind conditions (U_{10} >15 m s^{-1}) in the western Pacific :

$$k_{short} = 0.266\ U_{10}^2\ (Sc_{38}/600)^{-1/2} \tag{9}$$

More recently, a dependency of k on wind speed stronger than a quadratic relationship has been suggested. For instance, [68] suggested a cubic dependency of k on either short-term or long-term mean winds conditions (W-99 relationship) :

$$\begin{cases} k_{short} = 0.0283\ U_{10}^3\ (Sc_{38}/660)^{-1/2} \\ k_{long} = (1.09\ U_{10} - 0.333\ U_{10}^2 + 0.078\ U_{10}^3)\ (Sc_{38}/660)^{-1/2} \end{cases} \tag{10}$$

Finally, a formulation of k based on coastal ocean data has been also developed (N-00 relationship, [69]). N-00 expresses the k vs wind speed relationship

for data from the North Sea experiments. These were also combined with the data of two other studies on Georges Bank and on the West Florida Shelf using the same method to cover a wider range of wind speeds. Such multi-tracer experiment study lead to a second-order polynomial relationship for short-term wind conditions :

$$k_{short} = 0.222\ U_{10}^2 + 0.333\ U_{10}\ (Sc_{38}/660)^{-1/2} \tag{11}$$

Our time scales between two mappings (order of a day) suggest that the relations with short-term wind are likely to be the more appropriate. However, these relations assume steady wind conditions. In our case, the wind speed variability over the time period considered might be important. The average ship wind for the period from September 11 to September 18 is equal to 13.3 $m\ s^{-1}$ from the hourly data (Fig. 5-a) with a standard deviation of 6.7 $m\ s^{-1}$, showing a significant wind speed variability. In order to evaluate the impact of wind variability and asymmetry, following [70], we can derive two "enhancement factors":

$$\begin{aligned} \epsilon_2 &= \overline{U_{10}^2}/\overline{U_{10}}^2 \\ \epsilon_3 &= \overline{U_{10}^3}/\overline{U_{10}}^3 \end{aligned} \tag{12}$$

For each time period and for any given gas exchange-wind speed relationship, these enhancement factors can be used to assess the contribution of nonlinear dependencies in yielding higher or lower air-sea transfer velocities due to highly variable instantaneous winds ($k_{inst} = k_{obs}/\epsilon$) compared to steady ones. The values of ϵ_2 range from 0.46 (between the release and Mapping 1) to 1.27 (between Mapping 3 and Mapping 4). This implies that, if a quadratic dependency is assumed, the variation of the wind can reduce the gas exchange by 54 % or enhances it by 27 % during this time period compared with a steady wind. The values of ϵ_3 range from 0.74 to 1.87 for the same periods, respectively. This indicates that, if a cubic dependency is assumed, the asymmetry of the wind can reduce the gas exchange by 26 % or enhances it by 87 % compared with a steady wind.

4.2. Applications

We can now compare the evolution of the *in situ* quantity of SF_6 (black squares - Fig. 5-b) with the five proposed parameterizations. The atmospheric loss is estimated at about 0.27 mol d^{-1} between the release and Mapping 1 (Fig. 5-b). The calculated evaporation rate suggests that ~31 % of the released SF_6 is lost during this period, due to the observed increase of wind speed (Fig. 5-a). Between Mapping 1 and 2, ~57 % of the initial amount of SF_6 is further lost with a rate of 0.27 mol d^{-1} due to the persistent strong winds (20-25 m s^{-1} wind speed). Between Mapping 2 and 3, as wind speed decreases to ~4 m s^{-1}, the atmospheric loss declines to 0.01 mol d^{-1}. The temporal evolution of the wind speed (Fig. 5-a) clearly shows the link between the increase of wind and the decrease of total SF_6 within the patch.

Only two relationships are applicable to both short and long wind conditions (equation (8) W-92 and equation (10) W-99). We have evaluated the performance of these relationships by comparing the sum of squared residuals (RMS), computed as the difference between the observed and the modeled quantity of SF_6. Moreover, we computed a second estimate of the RMS in which an estimate of the standard deviation, associated with the error affecting each measure of SF_6 (± 5 %), is used to "weight" the contribution of each term within the sum. In both cases the minimum RMS is found for the short-term wind relationships (data not shown).

Hence, we compare the evolution of the quantity of SF_6 only with the five parameterizations based on short-term wind conditions (Fig. 5-b). The temporal variability of the measured total SF_6 is in good agreement with the empirical curves. Between the release and Mapping 1 (Mapping 3 and Mapping 4), the empirical curves show an underestimate (overestimate) of gas exchange. This can be explained by the enhancement factors due to the variance of the wind, which, as shown before, can substantially reduce (increase) the gas exchange. The N-00 relationship is the most accurate relationship for our data, closely followed by the Ho-06 one. The results show that two of the commonly used parameterizations, the piecewise linear relationship of LM-86 and the cubic re-

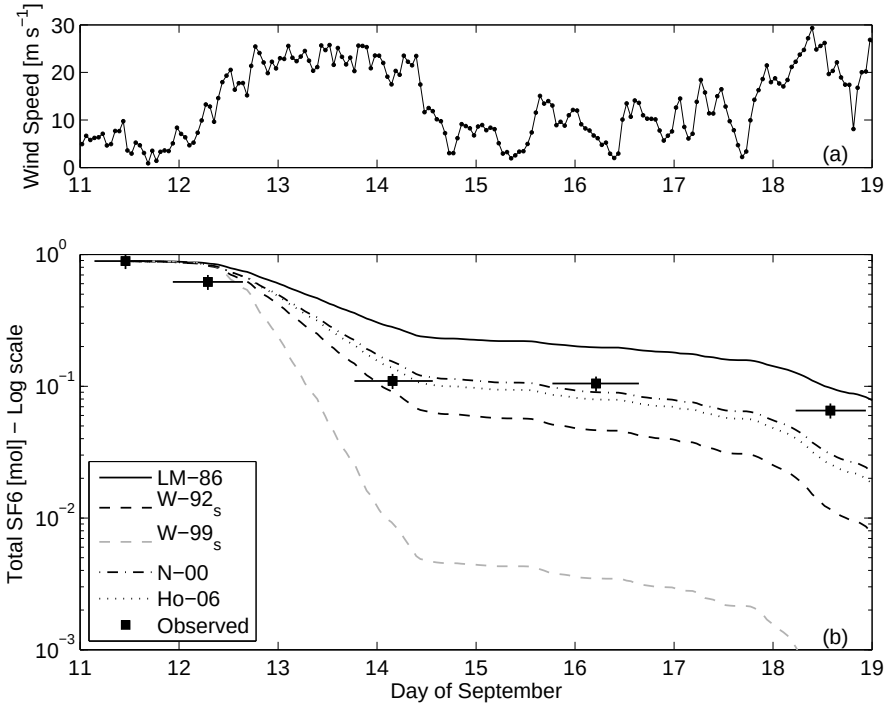

Figure 5: Temporal evolution of (a) the wind speed at 10 m above the sea level (U_{10}, [m s^{-1}]) as measured from the ship and (b, black squares) observed total SF_6 [mol]. The horizontal and verticallines over the black squares represent the estimated uncertainties on the calculation of total SF_6 associated to the wind variability, the depth of the mixed layer and the time dependence. They are always calculated but negligible when not visible. The different lines in (b) show the total SF_6 as predicted using the five different parametrization of the air-sea transfer velocity k. See text for details.

lationship of W-99, are inconsistent with measurements of gas transfer velocities at high and variable wind speeds for the coastal area of our study. The quadratic relationship of W-92 is better than the two previous ones.

5. Lateral diffusivity coefficients

The temporal evolution of the SF_6 patch can be used to quantify the lateral diffusivity coefficient. Various methods have been proposed to obtain this coef-

ficient.

We have seen that, between the release and Mapping 2, the sink term representing the atmospheric loss (last term in equation (1)) cannot be neglected. However, after Mapping 2, this sink term becomes very small and linear. Hence, neglecting it becomes a valid assumption (personal communication, Wanninkhof and Ledwell). The time between the release and Mapping 2 is likely sufficient for the complete mixing of SF_6 within the mixed layer (*i.e.* consistent with [55] who suggested a period of 48 h). Therefore, after one full day, equation (1) can be reduced to an effective horizontal diffusivity plus a large-scale horizontal strain.

As noted in Section 3, the tracer patch does not spread isotropically in the major and minor axis directions. Hence, only the methods based on anisotropic spreading are outlined. If we assume a Gaussian distribution, as considered in section 3, the concentration C as a function of space and time can be expressed as :

$$C = \frac{M}{\sigma_l \sigma_w} e^{-[(x^2/2\sigma_l^2)+(y^2/2\sigma_w^2)]} \tag{13}$$

with M, the total mass of tracer. Using this relation, the equations of the lengths of the major (σ_l) and minor (σ_w) axis of the SF_6 patch can be found by multiplying equation (1) by x^2, or by y^2, neglecting the atmospheric loss, and integrating over all x, or over all y [71, 26, 72]. σ_l and σ_w are thus governed by:

$$\frac{d\sigma_l^2}{dt} - 2\gamma\sigma_l^2 = 2K_h \tag{14}$$

$$\frac{d\sigma_w^2}{dt} + 2\gamma\sigma_w^2 = 2K_h \tag{15}$$

These equations can be solved considering different stages of the dispersion of the patch [73]. For a small initial patch, $(\sigma_l^2, \sigma_w^2) << \frac{K_h}{\gamma}$, the strain effects are negligible and equations (14) and (15) can be reduced to the simple Fickian horizontal diffusion model (Fickian model) :

$$K_h = \Delta\sigma_l^2/2\Delta t = \Delta\sigma_w^2/2\Delta t \tag{16}$$

where Δt is the difference between the central times of the different mappings. This calculation has been used in areas with different dynamical characteristics than our region of study (e.g. interiors of wide shelf sea), usually less energetic and/or away from coastal boundaries, shelf break and frontal features [20, 41]. Furthermore, in our case this method cannot be applied due also to the importance of the sink term at the beginning of the patch evolution.

For longer times, the strain of the patch cannot be neglected anymore, so that equations (14) and (15) have, respectively, the following solutions :

$$\sigma_l^2 = (\sigma_{l_0}^2 + \frac{K_h}{\gamma})e^{2\gamma t} - \frac{K_h}{\gamma} \tag{17}$$

$$\sigma_w^2 = (\sigma_{w_0}^2 - \frac{K_h}{\gamma})e^{-2\gamma t} + \frac{K_h}{\gamma} \tag{18}$$

with σ_{l_0} and σ_{w_0} the initial length of the patch along the directions of the major and minor axes, respectively This set of equations, known as the diffusion-strain model, allows us to calculate the strain rate (γ) and the effective horizontal diffusivity (K_h) using the values of σ_l and σ_w estimated in Section 3 [*e.g.* 19].

At later stages of the patch dispersion, its width can be hypothesized to be in a near-steady state, i.e. the thinning effect of the strain balances the widening tendency of diffusion (steady state model). This equilibrium can be reached when the time has been long enough so that the transient term, defined in the study of [26] as $e^{-2\gamma t}$, is negligible. This balance between the strain rate and the lateral diffusivity is based on the assumption that the currents in the surface ocean are approximately two-dimensional and divergence-free at scales greater than $\mathcal{O}(1)$ km, conditions typical for regions without intense sub-mesoscale features. In our case, the presence of a front is clearly identified. Nevertheless the assumptions may still hold because of its thermohaline characteristics. Indeed, [57] evidenced the compensated nature of the front, i.e., the horizontal gradient of temperature is balanced by the salinity gradient inducing small horizontal variation of density. Because of that, we can assume the dynamics associated with the front to be dominantly horizontal. At the near-steady state ($\frac{\partial \sigma_w^2}{\partial t} = 0$),

the equation for the minor-axis (15) can be written as :

$$K_h = \sigma_w^2 \gamma \tag{19}$$

In contrast, along the major axis, the length of the patch still increases exponentially at the rate γ and so :

$$\gamma = \frac{ln(\frac{\sigma_l(t+\Delta t)}{\sigma_l(t)})}{\Delta t} \tag{20}$$

As shown by [28] and [26], this calculation is valid until the horizontal scale of the tracer patch exceeds that of mesoscale eddies. Afterwards the exponential growth stops and the rate of dispersion of the patch can be modeled again as a diffusive process (as in equation (16)). In the area, the Rossby radius of deformation for typical stratified late-summer conditions is around 6 km, and mesoscale eddies are usually characterized by diameters between 20 and 30 km [74, 75].

In order to quantify the lateral diffusivity coefficients with both the diffusion-strain model and the steady state model, the lengths of the patch defined in section 3 are used. Two distinct conditions are required to apply these dispersal models. Both occurred during the second phase of the temporal evolution of the SF_6 patch discussed in section 3: a) starting at the beginning of Mapping 2, the sink term becomes negligible and the exponential growth of the patch is observed (stretching of the patch into a filament); b) the horizontal scales of the tracer patch (σ_w) for all mappings remained within the range typically observed for mesoscale features in the region. Therefore, the rate of dispersion can be adequately evaluated using the two models.

For the diffusion-strain model, the initial σ_{l_0} and σ_{w_0} have been defined with the characteristic of Mapping 2 (Table 2). Two σ_l and σ_w have been determined, one for Mapping 3 and one for Mapping 4. We do not consider the case between Mapping 3 and Mapping 4 because the time range between these two mappings was too short. Given these conditions, we can estimate the values γ and K_h corresponding to the intersection of the two curves representing, the solutions

of equation (17) and equation (18), respectively (Fig. 6-a,b). γ is estimated as 4.4 10^{-6} s^{-1} and K_h as 54.3 m^2 s^{-1} between Mapping 2 and Mapping 3 (Fig. 6-a). Between Mapping 2 and Mapping 4 (Fig. 6-b), γ is estimated as 2.5 10^{-6} s^{-1} and K_h as 23.2 m^2 s^{-1}.

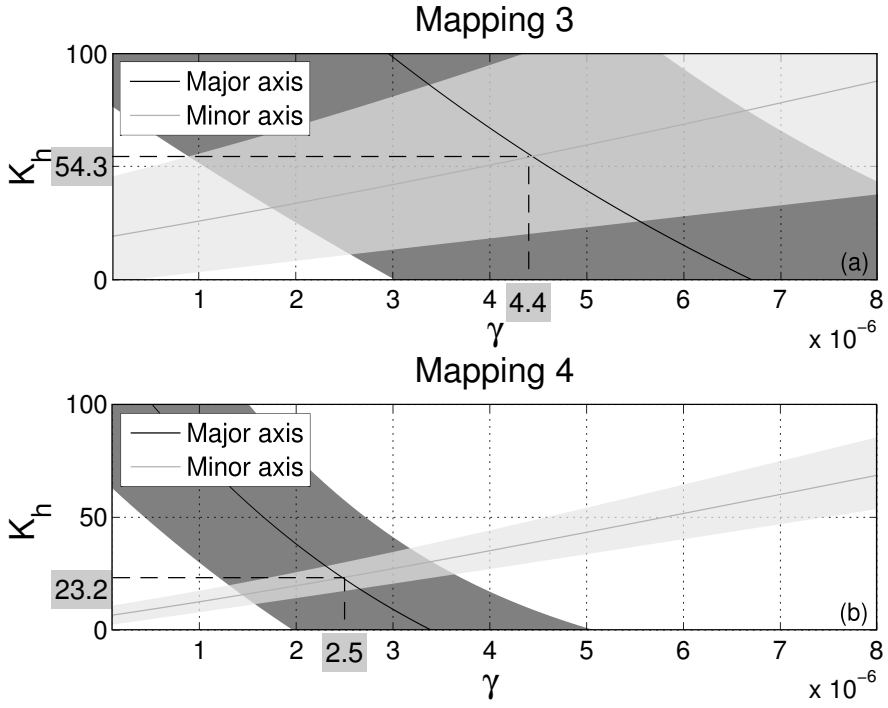

Figure 6: Graphic representation of possible combination of γ [s^{-1}] and K_h [m^2 s^{-1}] that could explain the observed growth of the tracer variance from Mapping 2 to Mapping 3 (a), and from Mapping 2 to Mapping 4 (b). The point of intersection of the two curves (equations (17) and (18 in the text) indicates the best estimates of γ and K_h. The shaded area represents the uncertainties.

Hypothesizing near-steady state conditions, we can also calculate γ and then K_h with the second model (equations (19) and (20)). Between Mapping 2 and Mapping 3, we find values for γ equal to 6.7 10^{-6} s^{-1} resulting in a K_h equal to 70.6 m^2 s^{-1}. Between Mapping 2 and Mapping 4, γ is equal to 3.4 10^{-6} s^{-1} and K_h equal to 29.0 m^2 s^{-1}. These different calculations, with associated

uncertainties, are resumed in Table 3.

Our results show large uncertainties in the diffusion-strain model results for K_h as well as large differences between the values of K_h obtained from the 2 methods between Mapping 2 and Mapping 3. We interpret these discrepancy as an indication that, at this stage, the filament has not yet reached a near-steady state, as also supported by a non negligible transient term. Moreover, the large uncertainties come from the larger errors associated with the Gaussian ellipsoids fits for Mapping 3.

Between Mapping 2 and Mapping 4, the transient term decreases to 0.15 and the estimate of K_h is similar for the two models with lower uncertainties. This implies that, although the adjustment has not taken place after two days (time interval between Mapping 2 and Mapping 3), it has occurred by Mapping 4, 4.5 days after Mapping 2. Thus the period of adjustment is in the range between 2 and 4.5 days. For this time scale, the transient term becomes negligible and the steady state model can be reasonably used.

Table 3: Estimates of the horizontal diffusivity coefficients and their variation ranges in square brackets with two models with the initial time corresponding to Mapping 2.

	Diffusion-Strain model		Steady state	
	γ (10^{-6} s^{-1})	K_h (m^2 s^{-1})	γ (10^{-6} s^{-1})	K_h (m^2 s^{-1})
Mapping 2 to Mapping 3	4.4 [2.6-5.3]	54.3 [11.1-114.0]	6.7 [6.4 - 7.3]	70.6 [34.7-119.0]
Mapping 2 to Mapping 4	2.5 [1.5-3.2]	23.2 [11.4-36.2]	3.4 [3.0 - 4.0]	29.0 [26.5-32.8]

6. Discussion and Concluding Remarks

The dynamics of a passive tracer has been studied in a coastal environment during the Latex10 campaign with a Lagrangian approach. Several studies have previously addressed the differences between an Eulerian approach and a Lagrangian one for the calculation of lateral diffusivity coefficient [76]. Generally, the results suggest that an Eulerian approach to calculate eddy diffusivities is most useful for satellite-derived velocity fields or for model outputs. On the other hand, if the measurements and the Lagrangian statistics are adequate, the calculation of eddy diffusivities from drifters trajectories or passive tracer release are the most accurate for in situ estimates. Nevertheless, obtaining adequate sampling of the tracer remains a crucial issue in coastal waters.

In our experiment, the tracer patch was followed for seven days, demonstrating the adequacy of the developed LATEXtools for tracer studies in a coastal environment. During and immediately after the release, the weak wind velocity ($4\ m\ s^{-1}$) led to an initial slow atmospheric loss. Therefore a good quantification of the total amount of SF_6 initially added to the surface mixed layer (0.89 ± 0.11 mol) is possible. We have tested different parameterizations of the ocean-atmosphere gas exchange. The good match between the empirical curves of the atmospheric loss and the total SF_6 mapped (Fig. 5) indicates a good coverage of the patch during the various mappings. The largest difference is observed for the total amount of SF_6 measured during Mapping 1. This underestimate of gas exchange in the empirical models can be due to the variance of the wind between the release and Mapping 1. Moreover, during that period, the hypothesis of homogeneity could not be completely respected as the time between the release and Mapping 1 ($<48\ h$) is not sufficient for the complete mixing of SF_6. Despite this underestimation, the formulation of [69], based on data collected in coastal ocean, has proved to be an effective parameterization of gas exchange in our study area.

The area of the tracer patch has been estimated considering two different calculations for the total area of the patch: the Gaussian ellipsoid method or

the contour line method. These methods are both based on the assumption of a Gaussian distribution of SF_6 concentration within the patch. They provided consistent results, with the contour line ones generally lower than the ellipsoid ones. This is probably due to the spatial resolution of the sampling that does not allow to find close contour lines for the reference value. Indeed, with this method, the tracer patch area is calculated summing multiple isolated patches, contradicting the Gaussian hypothesis. For this reason, in the following of the present paragraph we summarize the temporal evolution of the patch on the basis of the results obtained with the ellipsoid method. And we provide estimations of lateral diffusivity coefficients based on the lengths of the two axes of the ellipsoids.

Two phases can be distinguished in the temporal evolution of the SF_6 patch. The first phase corresponds to the time between the release and Mapping 2 (September 11 - 14, ~67 hours). During this phase, the total patch area initially spreads slowly to cover an area of 71±4 km^2 with a maximum concentration of SF_6 of 300±15 fmol L^{-1}. Furthermore, the patch remains trackable, despite the sudden increase of wind, starting on September 11 and reaching a maximum wind velocity of 25 m s^{-1} on September 13. The second phase of the temporal evolution of the patch corresponds to the time between Mapping 2 and Mapping 4 (September 14 - 18, ~105 hours). During that phase, the wind velocity suddenly decreases then increases again at the end of that period (Fig. 5-a). We observe that the total patch area increases linearly to eventually cover an area of 377±9 km^2 (Fig. 3-b). Maximum concentrations of SF_6 inside the total patch area are much smaller, with values between 45-60±3 fmol L^{-1}. In both phases, the evolution of the patch geometry (Fig. 3-c) shows a stretching of the patch into a filament.

Superimposing the distribution of the tracer on the pseudo-SST satellite image (Fig. 4) evidences the temporal evolution of the patch relative to the surrounding waters. Pseudo-SST satellite images were available for Mappings 1, 2 and 3 providing surface information on the dynamical patterns around the patch affecting its evolution. The presence of a front originating from the convergence of

warmer waters from the Northern Current and colder waters from the shelf has been discussed in [53]. The presence of the front clearly affects the patch during the second phase of its evolution, inducing its south-westward propagation from the continental shelf of the Gulf of Lion to the Catalan Basin. The presence of a front could affect the divergence-free assumption made for the calculation of the lateral diffusivity coefficients. However, this front has been identified as a compensated front [57], inducing dominantly horizontal dynamics.

In order to evaluate the lateral diffusivity coefficients from the SF_6 patch, we have used the diffusion-strain model and the steady state model. With the diffusion strain model, we obtained a γ of 2.5 10^{-6} s^{-1} and a K_h of 23.2 m^2 s^{-1} between Mapping 2 and Mapping 4, when the atmospheric loss of SF_6 can be neglected. The use of the steady state model can be limited by the near-steady state assumptions, which can be particularly constraining in highly dynamical coastal areas. At the same time, as no processes or structures in the ocean can truly reach a steady-state, the validity of such hypothesis is always relative to the scales of interests. In our case, we showed that an equilibrium could be reached when the time has been sufficiently long for the transient term to become negligible. After a period of adjustment between 2 and 4.5 days, the two models considered in this study converge to similar estimates. Therefore, after such time scale, the order of magnitude of the lateral diffusivity coefficient is not particularly sensitive to the further stretching of the patch.

The horizontal scales characterized by our method are defined by the width ($2\sigma_w$) of the SF_6 patch, equal to 11.8$\pm$1.4 km. The observed K_h of 23.2 m^2 s^{-1} is in the range of the typical value of 0.5-25 m^2 s^{-1} obtained by previous studies which combined estimates of the strain rate with *in situ* measurements of the patch width in high energetic systems [26, 27, 28, 29]. These estimates lie on the canonical diffusion diagram for spatial scales of order 10 km [4].

Our calculation of K_h includes hypotheses that are generally adopted for analogous experiments: namely, no air-sea loss of SF_6, and no vertical variations both in horizontal currents (shear) and in vertical diffusivity. The omission of air-sea loss is commonly used in the calculation of lateral diffusivity coefficient

as in the studies of [41] and [42]. Moreover it has been shown by [77] that the omission of air-sea loss and vertical shear in the horizontal currents results in some biases, but that they are small relative to other errors in the estimation of the lateral diffusivity coefficient. At the surface, we have assumed that the loss to the atmosphere does not affect the analysis. This hypothesis is valid since under the assumption that the SF_6 is homogeneous in the mixed layer the gas transfer velocity is independent of the position in the patch. Concerning the estimate of the exchanges at the bottom of the mixed layer, we observed that the pycnocline, representing the primary barrier to the vertical diffusion of SF_6, was well marked at about 23 m depth and remained constant during all the experiment.

Since lateral diffusivity coefficients are strongly influenced by local dynamics, comparing them with coefficients calculated for the same region represents a useful test for our estimate. During the Latex10 campaign, the analysis of the Lagrangian drifters trajectories and transects of surface temperature and salinity across the front allowed the retrieval of an independent series of estimates of K_h [57]. Their average K_h is 4 m^2 s^{-1} with 75 % of the values between 0.5 and 5 m^2 s^{-1} for horizontal scales in the order of 1 km. In both approaches, two assumptions are made : the large-scale strain field is steady and horizontally uniform, and the effects of cross-front mixing induced by small scale turbulence can be parameterized by an effective small-scale diffusivity. Although assuming similar hypotheses, the two methods differ by their spatial and temporal scales : the ones associated with the K_h computed in this study are larger (order of 10 km, and between 2 and 4.5 days) than in [57]. That could explain our larger values of K_h.

The lateral diffusivity coefficients have been estimated to a first order from the dynamics of a SF_6 patch in a coastal environment marked by the presence of small-scale dynamical features. The results are consistent with previous studies in open ocean. Thus, with an adapted sampling strategy, passive tracer experiments can be successfully applied also in coastal environments. Such experimental studies are crucial for better understanding the role of lateral diffusivity

in coastal areas with important mesoscale and submesoscale activity. They can provide critical support for further improving the accuracy of regional numerical models used for simulating and predicting the propagation of non-conservative tracers such as nutrients, plankton, and pollutants. Those are key factors in regulating the biological and ecological conditions of coastal region. Improving our understanding of the processes controlling environmental conditions of coastal regions has significant socio-economical implications, and represents a fundamental step towards their sustainable development.

7. Acknowledgments

The LATEX project was supported by the programs LEFE/IDAO and LEFE/CYBER of the CNRS/INSU-Institut National des Sciences de l'Univers and by the Region PACA-Provence Alpes Côte d'Azur. Francesco Nencioli acknowledges support from the FP7 Marie Curie Actions of the European Comission, via the Intra-European Fellowship (FP7-PEOPLE-IEF-2011), project Lyapunov Analysis in the COaSTal Environment (LACOSTE-299834). Users can access the data, available at the MIO Laboratory, from the PIs of the LATEX Project, A. A. Petrenko (anne.petrenko@univ-amu.fr) and F. Diaz (frederic.diaz@univ-amu.fr). The SST satellite data were kindly supplied by Météo-France. We are warmly grateful to the crews of the R/V Le Suroît and R/V Téthys II for their assistance. We thank Peggy Rimmelin, Anne Desnues and Marlène Ragot for their invaluable help with the SF_6. The authors thank Thierry Moutin and David Nerini for precious comments and useful discussions. We thank Dr. Ledwell and Dr. Sundermayer for helpful discussions, encouragement, and for taking the time to respond to our questions. The authors thank Dr. Wanninkhof and Dr. Abernathey, whose comments and suggestions greatly improved the quality of this work. The authors also thank the anonymous reviewers for their constructive remarks. Marion Kersalé was financed by a MENRT Ph.D. Grant.

Appendix A. Analytical system used for the analysis of SF6

The analytical system used for the analysis of SF_6 is based on a continuous flow purge and trap (PT) extraction followed by gas chromatography separation and detection by electron capture detector (GC/ECD). The analytical system is detailed in Fig. A1. We did not use vacuum sparge sample extraction, but continuous flow of purified nitrogen for extraction of dissolved gases. The water was sampled with a peristaltic pump in a laboratory sink, where surface water circulated after pumping by the ship for thermosalinometer measurements. The ship pump is situated 3 m under the surface. The PT sampling tubing was installed close to the arrival of the water (in the same bucket), in order to both prevent the water from degassing and minimize the dilution effect in the sink. The water flow entering the degassing system was fixed at 50 ml min^{-1}. This flow was adjusted manually in order to keep the degassing system full of water and to insure stability in the extraction efficiency. As the water circulated in the extractor, purified nitrogen (Alpha2 air liquid purified from oxygen, moisture and organic compounds) purged the water at a flow rate of 50 ml min^{-1}. The gas extracted was then desiccated through magnesium perchlorate powder and circulate in 10.47 ml loop. This volume was then injected every 3 min on a cold trap (-100°C ethanol) for three minutes. After 3 min, the trap was isolated (rotation of Va) and immerged in the hot bath (+100°C boiling water). The trap used was made in a 10 cm, $1/8^e$ inch diameter inox tube full with HayesepD phase. This trap allowed the total trapping of SF_6 and CFCs for more than 15 min at -100°C. After 20 s, Vb rotated and the gas trapped were desorbed and injected on a pre-column and on the analytical column for 40 s. After that time, Vb and Va came back to their initial positions. The gas injected was then separated and quantified by the GC/ECD (Perkin Elmer Clarus 500). The precolumn is a PLOT molecular sieve 5A, 1 m long and 0.53 mm diameter. The analytical column is the same but 10 m long. The precolumn protects the column from heavy compounds (VOCs), which could be difficult to elute. The GC oven was fixed at 70°C. The chromatographic analysis was

3 min long. The SF_6 extraction efficiency in continuous flow system was calculated and verified by regular analyses of the same water sampled at the same time by sampling ampoules and analyzed by classical PT-GC/ECD technique. The yield of extraction usually varied between 70 and 100 %, depending on the gas and water flow. For one mapping, the flow meter was accidentally partially blocked and extraction efficiency droped to 17 %. As our analytical system could also determine CFC-12 in the same time, our extraction efficiency was also verified for this parameter, which should stay constant in water (function of temperature and salinity). Standardization of the chromatographic system was realized twice a day, with an air standard (NOAA/CMDL standard, 2006 calibrated air) containing 5.76 pptv of SF_6. Air standard was injected in loops with various volumes (0.05 ml to 10 ml), in order to obtain a calibration curve. The calibration was linear from 0.2 fmol to more than 35 fmol. Calibration remained very stable throughout the entire campaign.

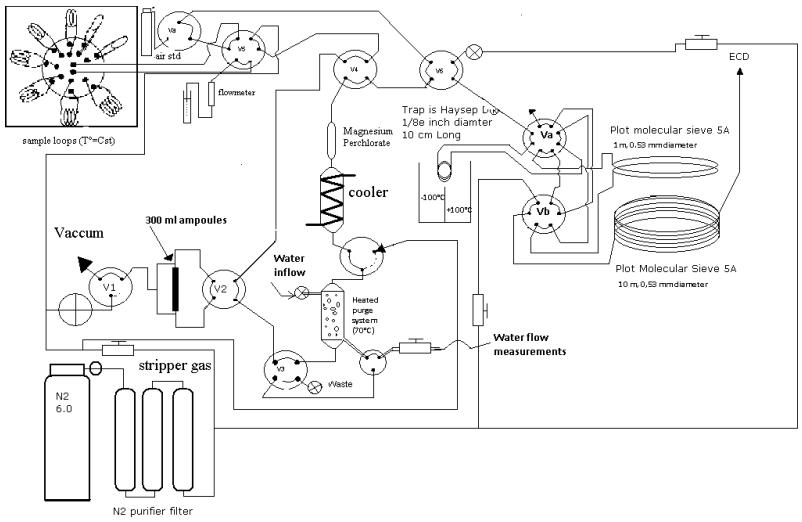

Figure A1: Analytical system used for the analysis of SF_6, based on continuous flow purge and trap (PT) extraction followed by gas chromatography separation and detection by electron capture detector (GC/ECD).

References

[1] L. F. Richardson, Atmospheric diffusion shown on a distance-neighbour graph, in: Proc. R. Soc. London, Series A., Vol. 110, 1926, pp. 709–737.

[2] L. F. Richardson, H. Stommel, Note on eddy diffusion in the sea, Journal of Meteorology 5 (5) (1948) 238–240.

[3] H. Stommel, Horizontal diffusion due to oceanic turbulence, J. Mar. Res. 8 (3) (1949) 199–225.

[4] A. Okubo, Oceanic diffusion diagrams, in: Deep sea research and oceanographic abstracts, Vol. 18, Elsevier, 1971, pp. 789–802.

[5] J. Smagorinsky, General circulation experiments with the primitive equations, i. the basic experiment, Mon. Wea. Rev. 91 (3) (1963) 99–164.

[6] I. James, Advection schemes for shelf sea models, J. Mar. Sys. 8 (1996) 237–254. doi:10.1016/0924-7963(96)00008-5.

[7] B. Fox Kemper, D. Menemenlis, Can Large Eddy Simulation Techniques Improve Mesoscale Rich Ocean Models?, American Geophysical Union, 2008, pp. 319–337. doi:10.1029/177GM19.

[8] A. Bracco, S. Clayton, C. Pasquero, Horizontal advection, diffusion, and plankton spectra at the sea surface, J. Geophys. Res. 114 (C2) (2009). doi:10.1029/2007JC004671.

[9] G. Holloway, Estimation of oceanic eddy transports from satellite altimetry, Nature 23 (1986) 243–244.

[10] R. Ferrari, M. Nikurashin, Suppression of Eddy Diffusivity across Jets in the Southern Ocean., J. Phys. Oceanogr. 40 (7) (2010).

[11] R. E. Davis, Observing the general circulation with floats, Deep-Sea Res. I 38 (1991) S531–S571.

[12] J. LaCasce, Statistics from Lagrangian observations, Prog. Oceanogr. 77 (1) (2008) 1–29.

[13] A. C. Haza, T. M. Özgökmen, A. Griffa, A. Molcard, P.-M. Poulain, G. Peggion, Transport properties in small-scale coastal flows: relative dispersion from VHF radar measurements in the Gulf of La Spezia, Ocean Dynam. 60 (4) (2010) 861–882.

[14] J. C. Ohlmann, J. H. LaCasce, L. Washburn, A. J. Mariano, B. Emery, Relative dispersion observations and trajectory modeling in the Santa Barbara Channel, J. Geophys. Res. 117 (C5) (2012) 1978–2012.

[15] K. Schroeder, J. Chiggiato, A. Haza, A. Griffa, T. Özgökmen, P. Zanasca, A. Molcard, M. Borghini, P.-M. Poulain, R. Gerin, et al., Targeted Lagrangian sampling of submesoscale dispersion at a coastal frontal zone, Geophys. Res. Lett. 39 (11) (2012).

[16] A. C. Poje, T. M. Özgökmen, B. L. Lipphardt, B. K. Haus, E. H. Ryan, A. C. Haza, G. A. Jacobs, A. Reniers, M. J. Olascoaga, G. Novelli, et al., Submesoscale dispersion in the vicinity of the Deepwater Horizon spill, Proceedings of the National Academy of Sciences 111 (35) (2014) 12693–12698.

[17] W. J. Emery, R. E. Thomson, Data analysis methods in physical oceanography, Elsevier Science, Amsterdam, 2001. doi:10.1016/B978-044450756-3/50000-9.

[18] W. Geyer, J. Ledwell, Final report: Massachusetts bay dye study, Mass. Water Resour. Auth., Charlestown, Mass. 17 (1994) 13 pp.

[19] M. A. Sundermeyer, J. R. Ledwell, Lateral dispersion over the continental shelf: Analysis of dye release experiments, J. Geophys. Res. 106 (C5) (2001) 9603–9621.

[20] M. E. Inall, D. Aleynik, C. Neil, Horizontal advection and dispersion in a stratified shelf sea: The role of inertial oscillations, Prog. Oceanogr. 117 (2013) 25–36.

[21] N. Stashchuk, V. Vlasenko, M. E. Inall, D. Aleynik, Horizontal dispersion in shelf seas: High resolution modelling as an aid to sparse sampling, Prog. Oceanogr. (2014) doi:10.1016/j.pocean.2014.08.007.

[22] R. J. Moniz, D. A. Fong, C. B. Woodson, S. K. Willis, M. T. Stacey, S. G. Monismith, Scale-dependent dispersion within the stratified interior on the shelf of northern Monterey Bay, J. Phys. Oceanogr. 44 (2013) 1049–1064.

[23] D. T. Ho, J. R. Ledwell, W. M. Smethie, Use of SF5CF3 for ocean tracer release experiments, Geophys. Res. Lett. 35 (4) (2008).

[24] D. Banyte, M. Visbeck, T. Tanhua, T. Fischer, G. Krahmann, J. Karstensen, Lateral diffusivity from tracer release experiments in the tropical north atlantic thermocline, J. Geophys. Res. (2013). doi:10.1002/jgrc.20211.

[25] P. L. Holtermann, L. Umlauf, T. Tanhua, O. Schmale, G. Rehder, J. J. Waniek, The baltic sea tracer release experiment: 1. mixing rates, J. Geophys. Res. 117 (C1) (2012). doi:10.1029/2011JC007439.

[26] J. R. Ledwell, A. J. Watson, C. S. Law, Mixing of a tracer in the pycnocline, J. Geophys. Res. 103 (C10) (1998) 21499–21529.

[27] T. Stanton, C. Law, A. Watson, Physical evolution of the IronEx-I open ocean tracer patch, Deep-Sea Res. II 45 (6) (1998) 947 – 975. doi:10.1016/S0967-0645(98)00018-6.

[28] E. Abraham, C. Law, P. Boyd, S. Lavender, M. Maldonado, A. Bowie, Importance of stirring in the development of an iron-fertilized phytoplankton bloom, Nature 407 (2000) 727–730.

[29] A. P. Martin, K. J. Richards, C. S. Law, M. Liddicoat, Horizontal dispersion within an anticyclonic mesoscale eddy, Deep-Sea Res. II 48 (45) (2001) 739 – 755. doi:10.1016/S0967-0645(00)00095-3.

[30] J. R. Ledwell, A. J. Watson, The Santa-Monica Basin tracer experiment - A study of dyapycnal and isopycnal mixing, J. Geophys. Res. 96 (C5) (1991) 8695–8718. doi:{10.1029/91JC00102}.

[31] R. E. Sonnerup, J. L. Bullister, M. J. Warner, Improved estimates of ventilation rate changes and CO2 uptake in the Pacific Ocean using chlorofluorocarbons and sulfur hexafluoride, J. Geophys. Res. 113 (C12) (2008). doi:10.1029/2008JC004864.

[32] A. Schneider, T. Tanhua, W. Roether, R. Steinfeldt, Changes in ventilation of the Mediterranean Sea during the past 25 yr 10 (4) (2013) 1405–1445. doi:10.5194/osd-10-1405-2013.

[33] T. Tanhua, D. W. Waugh, J. L. Bullister, Estimating changes in ocean ventilation from early 1990s CFC-12 and late 2000s SF_6 measurements, Geophys. Res. Lett. 40 (5) (2013) 927–932.

[34] C. Law, A. Martin, M. Liddicoat, A. Watson, K. Richards, E. Woodward, A Lagrangian SF_6 tracer study of an anticyclonic eddy in the North Atlantic: patch evolution, vertical mixing and nutrient supply to the mixed layer, Deep-Sea Res. II 48 (4-5) (2001) 705–724. doi:10.1016/S0967-0645(00)00112-0.

[35] J. Martin, K. Coale, K. Johnson, S. Fitzwater, R. Gordon, S. Tanner, C. Hunter, V. Elrod, J. Nowicki, T. Coley, et al., Testing the Iron Hypothesis in Ecosystems of the Equatorial Pacific-Ocean, Nature 371 (6493) (1994) 123–129.

[36] D. J. Cooper, A. J. Watson, P. D. Nigthingale, Large decrease in ocean-surface CO2 fugacity in response to in situ iron fertilization, Nature 383 (6600) (1996) 511–513.

[37] D. Tsumune, J. Nishioka, A. Shimamoto, S. Takeda, A. Tsuda, Physical behavior of the SEEDS iron-fertilized patch by sulphur hexafluoride tracer release, Prog. Oceanogr. 64 (2-4) (2005) 111–127. doi:10.1016/j.pocean.2005.02.018.

[38] D. Tsumune, J. Nishioka, A. Shimamoto, Y. W. Watanabe, T. Aramaki, Y. Nojiri, S. Takeda, A. Tsuda, T. Tsubono, Physical behaviors of the iron-fertilized patch in SEEDS II, Deep-Sea Res. II 56 (26) (2009) 2948–2957. doi:10.1016/j.dsr2.2009.07.004.

[39] C. Law, W. Crawford, M. Smith, P. Boyd, C. Wong, Y. Nojiri, M. Robert, E. Abraham, W. Johnson, V. Forsland, M. Arychuk, Patch evolution and the biogeochemical impact of entrainment during an iron fertilisation experiment in the sub-Arctic Pacific, Deep-Sea Res. II 53 (20-22) (2006) 2012–2033. doi:10.1016/j.dsr2.2006.05.028.

[40] G. Csanady, Circulation in the coastal ocean, D.Reidel Publishing Company, Kluwer Group, Dordrech, Holland, 1982.

[41] R. Wanninkhof, G. Hitchcock, W. J. Wiseman, G. Vargo, P. B. Ortner, W. Asher, D. T. Ho, P. Schlosser, M.-L. Dickson, R. Masserini, et al., Gas exchange, dispersion, and biological productivity on the west Florida shelf: Results from a Lagrangian tracer study, Geophys. Res. Lett. 24 (14) (1997) 1767–1770.

[42] M. Yang, S. Archer, B. Blomquist, D. Ho, V. Lance, R. Torres, Lagrangian evolution of DMS during the Southern Ocean gas exchange experiment: The effects of vertical mixing and biological community shift, J. Geophys. Res. 118 (12) (2013) 6774–6790.

[43] C. Millot, The Gulf of Lions' hydrodynamics, Cont. Shelf Res. 10 (1990) 885–894. doi:10.1016/0278-4343(90)90065-T.

[44] C. Albérola, C. Millot, J. Font, On the seasonal and mesoscale variabilities

of the Northern Current during the PRIMO-0 experiment in the western Mediterranean Sea, Oceanol. Acta 18 (2) (1995) 163–192.

[45] C. Sammari, C. Millot, L. Prieur, Aspects of the seasonal and mesoscale variabilities of the Northern Current inferred from the PROLIG-2 and PROS-6 experiments, Deep-Sea Res. I 42 (6) (1995) 893–917. doi:10.1016/0967-0637(95)00031-Z.

[46] A. A. Petrenko, Variability of circulation features in the Gulf of Lion NW Mediterranean Sea. Importance of inertial currents, Oceanol. Acta 26 (2003) 323–338.

[47] C. Estournel, X. Durrieu de Madron, P. Marsaleix, F. Auclair, C. Julliand, R. Vehil, Observation and modeling of the winter coastal oceanic circulation in the Gulf of Lion under wind conditions influenced by the continental orography (FETCH experiment), J. Geophys. Res. 108 (C3) (2003). doi:10.1029/2001JC000825.

[48] A. A. Petrenko, C. Dufau, C. Estournel, Barotropic eastward currents in the western Gulf of Lion, northwestern Mediterranean Sea, during stratified conditions, J. Mar. Sys. 74 (1-2) (2008) 406–428. doi:10.1016/j.jmarsys.2008.03.004.

[49] P. Conan, C. Millot, Variability of the Northern Current off Marseilles, western Mediterranean Sea, from February to June 1992, Oceanol. Acta 18 (2) (1995) 193–205.

[50] M. M. Flexas, X. Durrieu de Madron, M. A. Garcia, M. Canals, P. Arnau, Flow variability in the Gulf of Lions during the MATER HFF experiment (March-May 1997), J. Mar. Sys. 33-34 (2002) 197–214. doi:10.1016/S0924-7963(02)00059-3.

[51] A. A. Petrenko, Y. Leredde, P. Marsaleix, Circulation in a stratified and wind-forced Gulf of Lions, NW Mediterranean Sea: in situ and modeling data, Cont. Shelf Res. 25 (2005) 7–27. doi:10.1016/j.csr.2004.09.004.

[52] A. Doglioli, F. Nencioli, A. A. Petrenko, J.-L. Fuda, G. Rougier, N. Grima, A software package and hardware tools for in situ experiments in a Lagrangian reference frame, J. Atmos. Ocean. Tech. 30 (8) (2013). doi:10.1175/JTECH-D-12-00183.1.

[53] F. Nencioli, F. d'Ovidio, A. M. Doglioli, A. A. Petrenko, Surface coastal circulation patterns by in-situ detection of Lagrangian coherent structures, Geophys. Res. Lett. 38 (L17604) (2011). doi:10.1029/2011GL048815.

[54] R. Sugisaki, K. Taki, Simplified analyses of He, Ne, and Ar dissolved in natural waters, Geochemical Journal 21 (1) (1987) 23–27.

[55] J. S. Gulliver, B. Erickson, A. J. Zaske, K. S. Shimon, Measurement Uncertainty in Gas Exchange Coefficients, in: M. A. Donelan, W. M. Drennan, E. S. Saltzman, R. Wanninkhof (Eds.), Gas Transfer at Water Surfaces, American Geophysical Union, 2002, pp. 239–245. doi:10.1029/GM127p0239.

[56] Z. Y. Hu, A. A. Doglioli, A. M. Petrenko, P. Marsaleix, I. Dekeyser, Numerical simulations of eddies in the Gulf of Lion, Ocean Model. 28 (4) (2009) 203 – 208. doi:10.1016/j.ocemod.2009.02.004.

[57] F. Nencioli, F. d'Ovidio, A. Doglioli, A. Petrenko, In situ estimates of submesoscale horizontal eddy diffusivity across an ocean front, J. Geophys. Res. 118 (12) (2013) 7066–7080.

[58] C. Law, A. Watson, M. Liddicoat, Automated vacuum analysis of sulphur hexafluoride in seawater: derivation of the atmospheric trend (19701993) and potential as a transient tracer, Marine Chemistry 48 (1) (1994) 57 – 69. doi:10.1016/0304-4203(94)90062-0.

[59] T. Tanhua, K. Anders Olsson, E. Fogelqvist, A first study of SF_6 as a transient tracer in the Southern Ocean, Deep-Sea Res. II 51 (22) (2004) 2683–2699.

[60] R. Sibson, A brief description of natural neighbor interpolation, in: V. Barnett (Ed.), Interpreting Multivariate Data, John Wiley & Sons, New York, USA, 1981, pp. 21–36.

[61] M. d. Berg, O. Cheong, M. v. Kreveld, M. Overmars, Computational Geometry: Algorithms and Applications, 3rd Edition, Springer-Verlag TELOS, Santa Clara, CA, USA, 2008.

[62] P. Xiu, F. Chai, Modeling the effects of size on patch dynamics of an inert tracer., Ocean Science 6 (1) (2010).

[63] J. Lagarias, J. A. Reeds, M. H. Wright, W. P. E., Convergence Properties of the Nelder-Mead Simplex Method in Low Dimensions, SIAM Journal of Optimization 9 (1) (1998) 112–147.

[64] P. S. Liss, L. Merlivat, Air-sea gas exchange rates: Introduction and synthesis, in: The role of air-sea exchange in geochemical cycling, Springer, 1986, pp. 113–127.

[65] C. R. Wilke, P. Chang, Correlation of diffusion coefficients in dilute solutions, AIChE Journal 1 (2) (1955) 264–270. doi:10.1002/aic.690010222.

[66] R. Wanninkhof, Relationship between wind-speed and gas-exchange over the ocean, J. Geophys. Res. 97 (C5) (1992) 7373–7382. doi:10.1029/92JC00188.

[67] D. T. Ho, C. S. Law, M. J. Smith, P. Schlosser, M. Harvey, P. Hill, Measurements of air-sea gas exchange at high wind speeds in the southern ocean: Implications for global parameterizations, Geophys. Res. Lett. 33 (16) (2006).

[68] R. Wanninkhof, W. R. McGillis, A cubic relationship between air-sea CO2 exchange and wind speed, Geophys. Res. Lett. 26 (13) (1999) 1889–1892.

[69] P. D. Nightingale, G. Malin, C. S. Law, A. J. Watson, P. S. Liss, M. I. Liddicoat, J. Boutin, R. C. Upstill-Goddard, In situ evaluation of air-sea gas

exchange parameterizations using novel conservative and volatile tracers, Global Biogeochemical Cycles 14 (1) (2000) 373–387.

[70] R. Wanninkhof, K. F. Sullivan, Z. Top, Air-sea gas transfer in the Southern Ocean, J. Geophys. Res. 109 (C8) (2004) 1978–2012.

[71] A. Townsend, The diffusion of heat spots in isotropic turbulence, Proceedings of the Royal Society of London. Series A. Mathematical and Physical Sciences 209 (1098) (1951) 418–430.

[72] M. A. Sundermeyer, J. F. Price, Lateral mixing and the North Atlantic Tracer Release Experiment: Observations and numerical simulations of Lagrangian particles and a passive tracer, J. Geophys. Res. 103 (C10) (1998) 21481–21497. doi:10.1029/98JC01999.

[73] C. Garrett, On the initial streakness of a dispersing tracer in two-and three-dimensional turbulence, Dyn. Atmos. Oceans 7 (4) (1983) 265–277.

[74] Z. Y. Hu, A. A. Petrenko, A. M. Doglioli, I. Dekeyser, Study of mesoscale anticyclonic eddy in the western part of the Gulf of Lion, J. Mar. Sys. 88 (2011) 3–11. doi:10.1016/j.jmarsys.2011.02.008.

[75] M. Kersalé, A. M. Doglioli, A. A. Petrenko, I. Dekeyser, F. Nencioli, Physical characteristics and dynamics of the coastal Latex09 Eddy derived from in situ data and numerical modeling, J. Geophys. Res. 118 (2013) 1–11. doi:10.1029/2012JC008229.

[76] A. Klocker, R. Ferrari, J. H. Lacasce, S. T. Merrifield, Reconciling float-based and tracer-based estimates of lateral diffusivities, J. Mar. Sys. 70 (4) (2012) 569–602.

[77] C. S. Law, E. R. Abraham, A. J. Watson, M. I. Liddicoat, Vertical eddy diffusion and nutrient supply to the surface mixed layer of the antarctic circumpolar current, J. Geophys. Res. 108 (C8) (2003). doi:10.1029/2002JC001604.